



HAL
open science

The Chemical Nature of Orion Protostars: Are ORANGES Different from PEACHES? ORANGES II.

Mathilde Bouvier, Cecilia Ceccarelli, Ana López-Sepulcre, Nami Sakai,
Satoshi Yamamoto, Yao-Lun Yang

► To cite this version:

Mathilde Bouvier, Cecilia Ceccarelli, Ana López-Sepulcre, Nami Sakai, Satoshi Yamamoto, et al..
The Chemical Nature of Orion Protostars: Are ORANGES Different from PEACHES? ORANGES
II.. The Astrophysical Journal, 2022, 929, 10.3847/1538-4357/ac5904 . insu-03705359

HAL Id: insu-03705359

<https://insu.hal.science/insu-03705359>

Submitted on 27 Jun 2022

HAL is a multi-disciplinary open access archive for the deposit and dissemination of scientific research documents, whether they are published or not. The documents may come from teaching and research institutions in France or abroad, or from public or private research centers.

L'archive ouverte pluridisciplinaire **HAL**, est destinée au dépôt et à la diffusion de documents scientifiques de niveau recherche, publiés ou non, émanant des établissements d'enseignement et de recherche français ou étrangers, des laboratoires publics ou privés.



Distributed under a Creative Commons Attribution 4.0 International License



The Chemical Nature of Orion Protostars: Are ORANGES Different from PEACHES? ORANGES II.

Mathilde Bouvier¹ , Cecilia Ceccarelli¹ , Ana López-Sepulcre^{1,2} , Nami Sakai³ , Satoshi Yamamoto^{4,5} , and Yao-Lun Yang^{3,6}

¹ Univ. Grenoble Alpes, CNRS, IPAG, 38000 Grenoble, France; mathilde.bouvier@univ-grenoble-alpes.fr

² Institut de Radioastronomie Millimétrique (IRAM), 300 rue de la Piscine, 38400 Saint-Martin d'Hères, France

³ RIKEN Cluster for Pioneering Research, 2-1 Hirosawa, Wako-shi, Saitama 351-0198, Japan

⁴ Department of Physics, The University of Tokyo, 7-3-1, Hongo, Bunkyo-ku, Tokyo 113-0033, Japan

⁵ Research Center for the Early Universe, The University of Tokyo, 7-3-1, Hongo, Bunkyo-ku, Tokyo 113-0033, Japan

⁶ Department of Astronomy, University of Virginia, Charlottesville, VA 22904-4235, USA

Received 2021 October 11; revised 2022 February 25; accepted 2022 February 26; published 2022 April 8

Abstract

Understanding the chemical past of our Sun and how life appeared on Earth is no mean feat. The best strategy we can adopt is to study newborn stars located in an environment similar to the one in which our Sun was born and assess their chemical content. In particular, hot corinos are prime targets because recent studies have shown correlations between interstellar complex organic molecules abundances from hot corinos and comets. The ORion ALMA New GEneration Survey aims to assess the number of hot corinos in the closest and best analog to our Sun's birth environment, the OMC-2/3 filament. In this context, we investigated the chemical nature of 19 solar-mass protostars and found that 26% of our sample sources show warm methanol emission indicative of hot corinos. Compared to the Perseus low-mass star-forming region, where the PERseus ALMA CHEMistry Survey detected hot corinos in $\sim 60\%$ of the sources, the hot corinos seem to be relatively scarce in the OMC-2/3 filament. While this suggests that the chemical nature of protostars in Orion and Perseus is different, improved statistics is needed in order to consolidate this result. If the two regions are truly different, this would indicate that the environment is likely playing a role in shaping the chemical composition of protostars.

Unified Astronomy Thesaurus concepts: [Astrochemistry \(75\)](#); [Protostars \(1302\)](#); [Star formation \(1569\)](#); [Chemical abundances \(224\)](#)

1. Introduction

Understanding how life appeared on Earth is one of the holy grails in science. From an astrophysical point of view, as the Sun's birth environment being long dissipated, we cannot see what happened in its youth. We can, however, study solar-mass protostars that are currently forming in other regions of our Galaxy to understand the full story of our planetary system formation.

The discovery of two chemically distinct types of solar-mass protostars—hot corinos and warm carbon-chain chemistry (WCCC) sources—shows that the story might not be the same for every solar-mass protostar. While hot corinos are compact (≤ 100 au), hot (≥ 100 K), and dense ($\geq 10^7 \text{ cm}^{-3}$) regions (Ceccarelli 2004; Ceccarelli et al. 2007), enriched in interstellar complex organic molecules (iCOMs; Herbst & Van Dishoeck 2009; Ceccarelli et al. 2017), WCCC objects are deficient in iCOMs but show a larger zone (~ 2000 au) enriched in unsaturated carbon-chain molecules (Sakai et al. 2008; Sakai & Yamamoto 2013). In between these two extreme cases, there exist objects called hybrids that present both hot corino and WCCC features (e.g., L483, B335; Imai et al. 2016; Oya et al. 2017; Jacobsen et al. 2019).

Until recently, only a dozen hot corinos were discovered, but thanks to the arrival of powerful (sub)millimeter interferometers such as ALMA, more hot corinos have been identified. In

particular, the recent Perseus ALMA Chemistry Survey (PEACHES; Yang et al. 2021) targeted 50 solar-mass protostars in the Perseus Molecular Cloud, a region forming only low-mass stars. They found that $\sim 56\%$ of their source sample show warm methanol emission, indicating that hot corinos are likely prevailing in this region. The Perseus Molecular Cloud is, however, different from the solar birth environment. The latter was most likely a dense protocluster with high-mass stars in its vicinity (e.g., Adams 2010; Pfalzner et al. 2015). Are hot corinos also abundant in an environment analog to that where our Sun was born? Recent studies showed similarities between the abundances of iCOMs found in hot corinos compared to those found in comets (Bianchi et al. 2019; Drozdovskaya et al. 2019; Rivilla et al. 2020). Did our Sun experience a hot corino phase? We need to target low-mass protostars belonging to massive star-forming regions (SFRs).

The closest and best analog of our Sun's birth environment is the OMC-2/3 filament, located in the Orion A molecular cloud. Very recently, three hot corinos were detected in this region, the intermediate-mass protostars HOPS-87 (also known as MMS6) and HOPS-370 (also known as OMC-2-FIR3) (Tobin et al. 2019; Hsu et al. 2020) and the solar-type protostar HOPS-108 located in the OMC-2 FIR4 protocluster (Tobin et al. 2019; Chahine et al. 2022). Although hot corinos are present in massive SFRs (Codella et al. 2016; Hsu et al. 2020; Chahine et al. 2022), the statistics is too poor to draw any conclusion on the chemical past of our Sun. We, therefore, need more systematic studies of hot corinos in massive SFRs.

The ORion ALMA New GEneration Survey (ORANGES) is a project aiming to study the chemical nature of the solar-type

protostars located in the OMC-2/3 filament, (393 ± 25) pc from the Sun (Großschedl et al. 2018), with an angular resolution of $0''.25$ (~ 100 au). ORANGES is analogous to PEACHES because the two studies have been designed to have the same sensitivity (corrected for the distance), spatial resolution, and spectral setup. It allows a direct comparison of the two environments, i.e., the OMC-2/3 filament and the Perseus Molecular Cloud. One of the goals of ORANGES is to assess the number of hot corinos in the OMC-2/3 region and provide a first answer concerning the chemical past of our Sun. In ORANGES, we targeted the same protostars targeted by Bouvier et al. (2021). These were initially nine chosen protostellar sources based on single-dish studies (e.g., Chini et al. 1997; Lis et al. 1998; Nielbock et al. 2003) satisfying the following three criteria: (1) detection in the (sub)millimeter continuum emission; (2) estimated envelope mass $\leq 12 M_{\odot}$; and (3) bona fide Class 0 and I protostars (see Bouvier et al. 2020). Recent interferometric studies showed that most of these systems are in fact multiple systems (Tobin et al. 2020; Bouvier et al. 2021), which led to a total number of 19 studied targets.

The results of a previous single-dish study (Bouvier et al. 2020) toward the same targets showed that the large-scale ($\leq 10^4$ au) line emission is dominated by the photodissociation region or by the molecular cloud, rather than the protostellar envelopes. Interferometric observations are thus essential to detect hot corinos in this highly illuminated region. In this study, we investigated the most common tracer of hot corinos, CH_3OH , in a sample of 19 embedded solar-type protostars. Table A1 lists the targeted protostars and their coordinates.

2. Observations

The observations were performed between 2016 October 25 and 2017 May 5 during Cycle 4, under ALMA project 2016.1.00376.S. The observations were performed in Band 6 using two different spectral setups. The ranges of frequencies covering the methanol transitions relevant for this work are 243.88–243.97 GHz and 261.77–261.88 GHz for setup 1, and 218.38–218.50 GHz, 230.33–234.08 GHz, and 234.64–234.76 GHz for setup 2. For setup 1, a total of 41 antennas of the 12 m array were used with a baseline length range of 18.6–1100 m. The integration time is ~ 20 minutes per source. For setup 2, a total of 45 antennas of the 12 m array were used with a baseline range of 18.6–1400 m. The integration time is ~ 8 minutes per source. The ALMA correlator was configured to have both narrow and wide spectral windows (spws), with 480 and 1920 channels, respectively. Narrow spws have a bandwidth of 58.59 MHz with a channel spacing of 122 kHz (~ 0.15 – 0.17 km s $^{-1}$), while the wide spws have a bandwidth of 1875 MHz with a channel spacing of 0.977 MHz (~ 1.2 – 1.3 km s $^{-1}$). The bandpass and flux calibrators were J0510 + 1800 and J0522–3627, and the phase calibrators were J0607–0834 and J0501–0159. The flux calibration error is estimated to be better than 10%. The precipitable water vapor (PWV) was typically less than 1 mm and the phase rms noise less than 60° . In the context of the ORANGES project, several molecular species were targeted but we focus here in particular on methanol (CH_3OH), the typical tracer of hot corinos. The methanol lines were found in six (both narrow and wide) spws. The rest frequencies of the methanol transition lines and the associated primary beam sizes are shown in Table A2.

We used the Common Astronomy Software Application (CASA; McMullin et al. 2007) for the data calibration. We then

exported the calibrated visibility tables to GILDAS⁷ format and performed the imaging in MAPPING. We first produced a continuum image by averaging line-free channels in the visibility plane using an automatic procedure. We then subtracted the continuum from the line emission directly in the visibility plane. We cleaned the cubes using natural weighting (with the CLEAN procedure) down to ~ 24 mJy beam $^{-1}$ on average. The phase self-calibration performed on the continuum of the sources (see Bouvier et al. 2021) has been applied to the cubes. The narrow spws were resampled to a channel spacing of 0.5 km.s $^{-1}$. The maps shown in this paper are not corrected for the primary beam attenuation but we took into account the correction to measure the line intensities. The resulting synthesized beam and rms for each source and each spectral window are presented in Table B1.

3. Results

3.1. Methanol Lines

Methanol is detected toward the center of 5 out of the 19 protostars: CSO33-b-a, FIR6c-a, MMS9-a, MMS5, and SIMBA-a. In these sources, the line spectra were extracted from the pixel corresponding to the position of the methanol peak, which often corresponds to the continuum emission peak. The coordinates of the position where the spectra have been extracted are indicated in Table A1. The line detection threshold is set to 3σ at the line emission peak. Figures 1 and 2 show the moment 0 map of the two CH_3OH lines at 243915 MHz and 234698 MHz, which have different upper-level energies E_u , overlaid on the 1.3mm dust continuum emission of each source. We note that for CSO33-b-a and SIMBA-a, the methanol transition at 234698 MHz ($E_u = 122.7$ K) is considered undetected as the emission is shown only by a 3σ contour, which is not centered on the source's continuum peak. We found that while the emission of methanol lines with low upper-level energy, such as the 243915 MHz transition, is resolved and extended in most sources, the emission of methanol lines with high upper-level energy, such as the 234,698 MHz transition, is compact. Methanol emission is seen near other sources of the sample but not at the position of the protostars. As we are interested in detecting hot corinos, we will focus in this letter only on the five sources cited above.

We detected up to 11 CH_3OH lines with upper-level energies E_{up} from 28 to 537 K and Einstein coefficients A_{ij} between 6.3×10^{-6} and 1×10^{-4} s $^{-1}$. The extracted spectra of methanol lines for each source are shown in Figure 3. We performed a Gaussian line fitting to each source in order to extract the line width (FWHM) and the peak velocity (V_{peak}). To extract the integrated intensity, we did a Gaussian fit ($\int T_B dV$ G.) and we also measured it by direct integration of the channel intensities ($\int T_B dV$ D). Only MMS5 has lines with Gaussian profiles so we used the Gaussian fit results for this source and the results of the direct integration for the other sources. The line-fitting results, as well as the rms computed for each spw, are reported in Table B1. Line widths range between ~ 2 and 7 km s $^{-1}$.

Methanol lines can be very optically thick toward hot corinos (Bianchi et al. 2020). We therefore looked for the isotopologue $\text{CH}_3^{18}\text{OH}$, which is usually optically thin, in order to derive the methanol column density more accurately. Among the seven $\text{CH}_3^{18}\text{OH}$ lines expected to be the most intense, we

⁷ <http://www.iram.fr/IRAMFR/GILDAS>

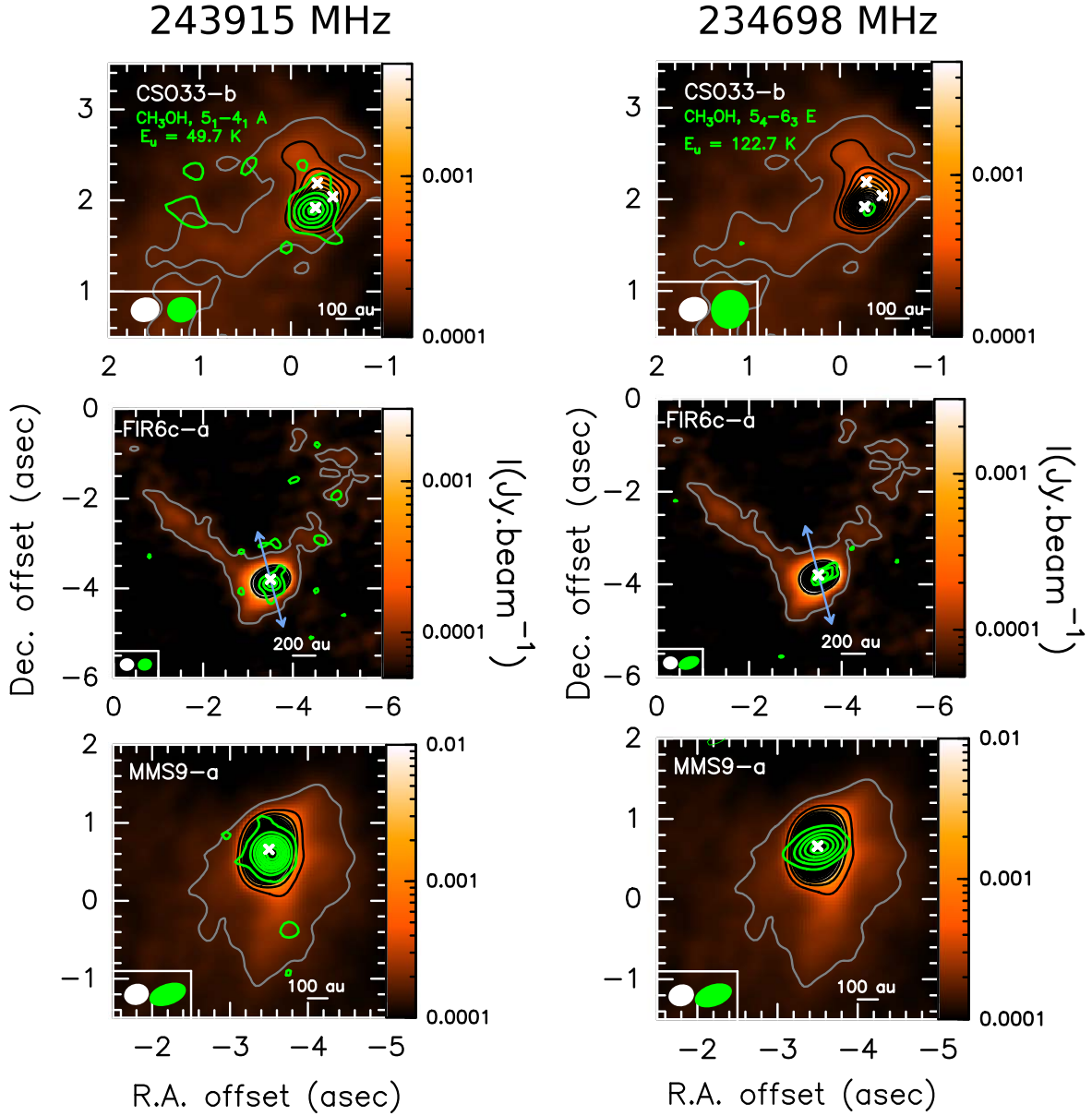


Figure 1. 1.3mm continuum maps of CSO33-b-a, FIR6c-a, and MMS9-a (colored area, gray and black contours). The first contour levels are in gray. Levels start at 15σ for CSO33-b-a ($1\sigma = 44 \mu\text{Jy beam}^{-1}$) and FIR6c-a ($1\sigma = 60 \mu\text{Jy beam}^{-1}$), and 20σ for MMS9-a ($1\sigma = 50 \mu\text{Jy beam}^{-1}$). Level steps are 50σ except for CSO33-b-a where the step is 10σ . The moment 0 emission of the CH_3OH transitions at 243915 MHz ($E_u = 49.7 \text{ K}$) and at 234698 MHz ($E_u = 122.7 \text{ K}$) is shown with green contours in the left and right columns, respectively. For the 243915 MHz transition line, contours start at 3σ ($1\sigma = 6, 9, 8 \text{ mJy beam}^{-1} \text{ km s}^{-1}$ for CSO33-b-a, FIR6c-a, and MMS9-a, respectively) with steps of 3σ for CSO33-b-a and FIR6c-a and steps of 5σ for MMS9-a. For the 234698 MHz transition line, contours start at 3σ ($1\sigma = 9, 9, 12 \text{ mJy beam}^{-1} \text{ km s}^{-1}$ for CSO33-b-a, FIR6c-a, and MMS9-a, respectively) with steps of 1σ for CSO33-b-a and FIR6c-a and 3σ for MMS9-a. The continuum- and methanol-associated synthesized beams are in white and green, respectively, and are depicted in the lower-left corner of the boxes. Light blue arrows represent the orientation of the outflow of the source when known (e.g., Williams et al. 2003; Takahashi et al. 2008; Shimajiri et al. 2009; Gómez-Ruiz et al. 2019; Tanabe et al. 2019; Feddersen et al. 2020). White crosses represent the position of the sources.

detected and used only one line. The other lines are either undetected ($\leq 3\sigma$) or contaminated by lines from other molecules such as $\text{C}_2\text{H}_5\text{OH}$, $\text{C}_2\text{H}_5\text{CN}$, or CH_2DOH . The spectral parameters and Gaussian fit results of the transition used in this work, which is the $5_{0,5}-4_{0,4} \text{ A}$ transition at 231758 MHz, are reported in Table B1. The frequencies of the seven $\text{CH}_3^{18}\text{OH}$ spectral lines expected to be the most intense are indicated in Figure B1.

3.2. Non-LTE LVG Analysis

To derive the physical properties of the gas where methanol is emitted, we performed a non-LTE analysis using the large velocity

gradient (LVG) code *grelvg*, originally developed by Ceccarelli et al. (2003). We used the $\text{CH}_3\text{OH}-\text{H}_2$ collisional rates from Flower et al. (2010) between 10 and 200 K for the first 256 levels, provided by the BASECOL database⁸ (Dubernet et al. 2013). We assumed a spherical geometry to compute the line escape probability (de Jong et al. 1980), a ratio $\text{CH}_3\text{OH-E}/\text{CH}_3\text{OH-A}$ equal to 1, and an H_2 ortho-to-para ratio of 3. The assumed line widths are those measured from the spectral lines toward each source (see Table B1), and we included the calibration error of 10% in the observed intensities.

⁸ <https://basecol.vamdc.eu/>

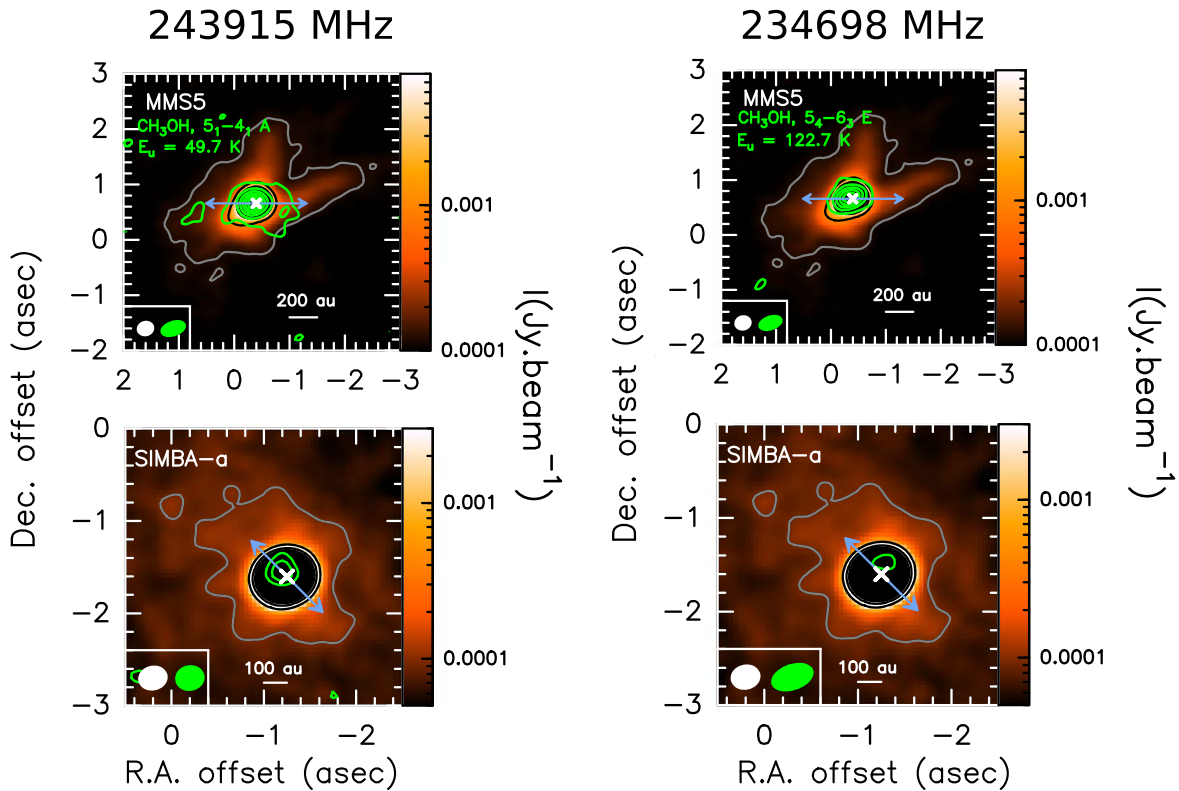


Figure 2. 1.3mm continuum maps for MMS5 and SIMBA-a (colored area, gray and black contours). The first contour levels are in gray. Levels start at 15σ for MMS5 ($1\sigma = 80 \mu\text{Jy beam}^{-1}$) and 10σ for SIMBA-a ($1\sigma = 50 \mu\text{Jy beam}^{-1}$). Level steps are 50σ . The moment 0 emission of the CH_3OH transitions at 243915 MHz ($E_u = 49.7$ K) and at 234698 MHz ($E_u = 122.7$ K) is shown with green contours in the left and right columns, respectively. For the 243915 MHz transition line, contours start at 3σ ($1\sigma = 7$ and $5 \text{ mJy beam}^{-1} \text{ km s}^{-1}$ for MMS5 and SIMBA-a, respectively) with steps of 10σ for MMS5 and 1σ for SIMBA-a. For the 234698 MHz transition line, contours start at 3σ ($1\sigma = 10$ and $7 \text{ mJy beam}^{-1} \text{ km s}^{-1}$ for MMS5 and SIMBA-a, respectively) with steps of 5σ for MMS5 and 1σ for SIMBA-a. The continuum- and methanol-associated synthesized beams are in white and green, respectively, and are depicted in the lower-left corner of the boxes. Light blue arrows represent the orientation of the outflow of the source when known (e.g., Williams et al. 2003; Takahashi et al. 2008; Gómez-Ruiz et al. 2019; Matsushita et al. 2019; Tanabe et al. 2019; Feddersen et al. 2020). White crosses represent the position of the sources.

The detected methanol transitions span a large range of E_{up} . First, methanol lines with E_{up} higher than 400 K have been excluded from the analysis as the collisional coefficients are not computed at these energies. Second, low-energy transitions can eventually trace a different region than the higher-energy-level transitions. Indeed, the low upper-energy-level transitions ($E_u \leq 50$ K) show extended emission toward most of the sources, while the high upper-level ones are compact. We, therefore, did not consider the low upper-energy lines when performing the LVG analysis, except for CSO33-b-a and SIMBA-a where we detected only three low-level energy transitions. Additionally, the line at 232418 MHz ($E_u = 165$ K) is likely contaminated by a $^{33}\text{SO}_2$ line falling at the same frequency. We do not have enough information (i.e., other lines) to evaluate the possible contribution of this line. We thus excluded this line from the LVG analysis as well.

In the case of MMS5, we also included the detected line of $\text{CH}_3^{18}\text{OH-A}$ with the $^{18}\text{O}/^{16}\text{O}$ ratio equal to 560 (Wilson & Rood 1994) to better constrain the derived total CH_3OH column density for this source. For each source, the lines that are not used for the LVG analysis are shown in italics in Table B1. In most cases, we ran the LVG radiative transfer code with only three lines so that the accuracy of the fit is not very elevated.

For each source, we ran a large grid of models varying the total ($\text{CH}_3\text{OH-E} + \text{CH}_3\text{OH-A}$) column density from 2×10^{14} to $3 \times 10^{19} \text{ cm}^{-2}$, the gas temperature from 20 to 200 K, and

the H_2 density from 3×10^5 to $1 \times 10^{10} \text{ cm}^{-3}$. These ranges for the parameters are those expected in hot corinos and in outflow shocks, as we expect emission coming from either of these two types of environments. We fitted the measured $\text{CH}_3\text{OH-E}$ and $\text{CH}_3\text{OH-A}$ line intensities simultaneously via comparison with the LVG model predictions, leaving $N_{\text{CH}_3\text{OH}}$, n_{H_2} , T_{kin} , and the source size (θ) as free parameters. Then, because the lines are optically thin in the cases of CSO33-b-a and SIMBA-a, there is a degeneracy between the source size and the column density, and the best fit of the LVG analysis actually provides the product $\theta \times N_x$. For these sources, we reran the best-fitting procedure, this time by fixing the source size and leaving $N_{\text{CH}_3\text{OH}}$, n_{H_2} , and T_{kin} as free parameters. We then varied the source size around its best-fit value to find when the $\theta \times N_x$ product does not give the same chi square, namely, where the degeneracy disappears.

The best fit for the total CH_3OH column densities ranges between 8×10^{15} and $4 \times 10^{18} \text{ cm}^{-2}$ with reduced χ_{red}^2 between 0.1 and 1.6. All the lines for CSO33-b-a and SIMBA-a, and the $\text{CH}_3^{18}\text{OH}$ line for MMS5 are optically thin ($\tau_L \leq 1$; τ_L being the line optical depth). For the other sources, methanol lines are mostly optically thick (FIR6c-a: $\tau_L = [1.1 - 5.2]$, MMS9-a: $\tau_L = [1.2 - 5.7]$, MMS5: $\tau_L = [0.9 - 4.2]$). The derived gas temperature and density are ≥ 85 K and $\geq 3 \times 10^6 \text{ cm}^{-3}$ for all sources, with the highest gas density for CSO33-b-a and the lowest gas density for FIR6c-a. The highest gas temperature is derived toward MMS9-a (≥ 130 K). The

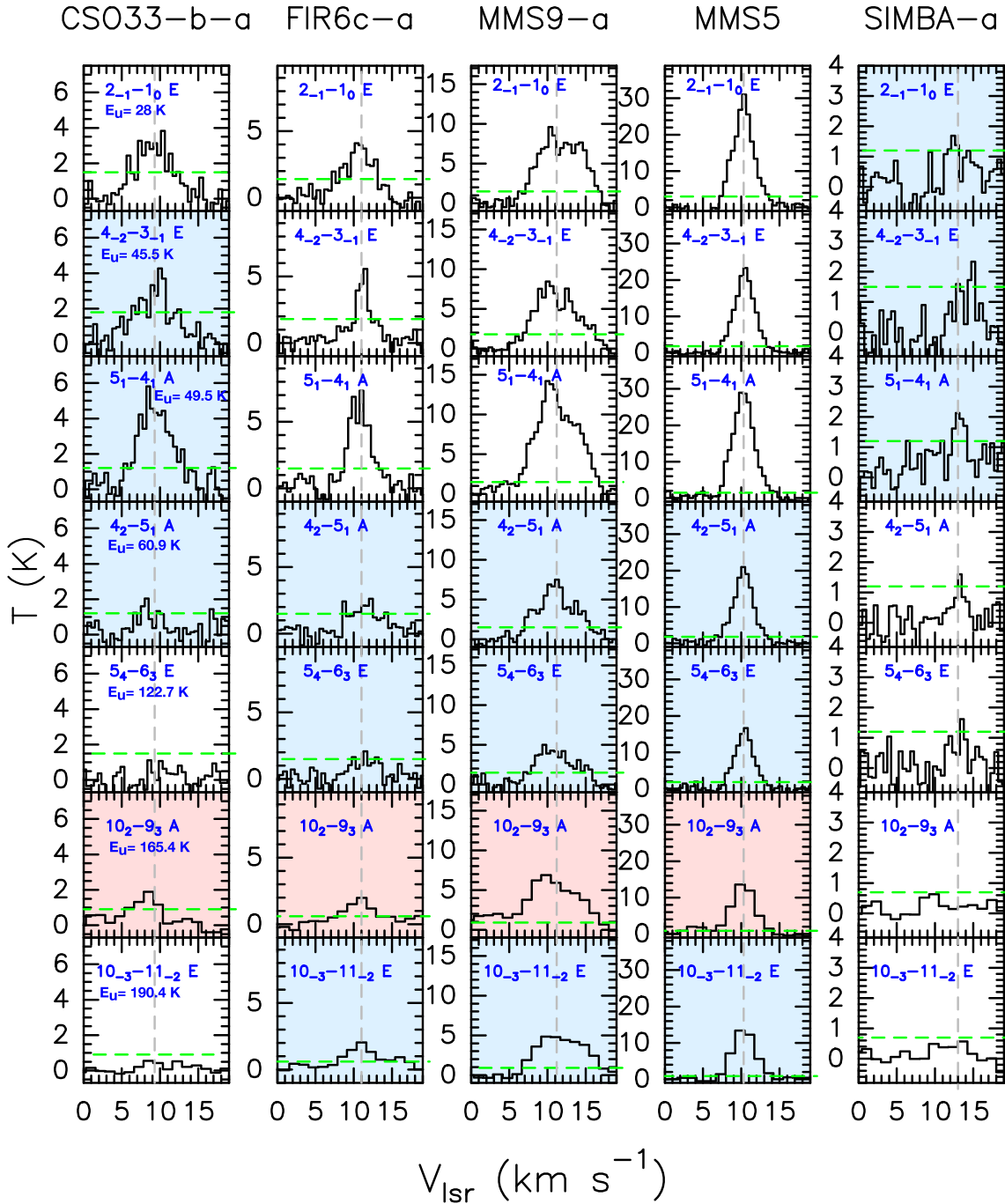


Figure 3. Methanol spectral lines detected in each source. The lines taken into account in the LVG analysis have a blue background. The lines with the red background are likely contaminated by a line of $^{33}\text{SO}_2$ and are thus left out from the LVG analysis. The transition of each line is marked in the top-left corner of the boxes. Dashed green lines show the 3σ level and dashed gray lines the averaged fitted peak velocity of all transitions of the associated source, V_{peak} , determined from the Gaussian line fitting.

observed lines are predicted to be emitted by sources between 0.07 and $0''.6$ (~ 28 – 236 au) in diameter. Figure 4 shows as an example the result of the LVG fit for MMS5. The best-fit solutions and ranges obtained for each source are reported in Table 1.

3.3. LTE versus Non-LTE analysis

We provide the results we obtained with the rotational diagram method (LTE) using the same lines as in the LVG

analysis in Table 1, in Figure C1. Depending on the sources, the LTE and non-LTE analyses can give similar or different results. In the cases of FIR6c-a and MMS9, the column densities can differ by up to two orders of magnitude. However, this is because, for these sources, we did not know a priori the size of the emitting region, and we thus used the sizes from Bouvier et al. (2021), which happened to be larger (up to $\sim 40\%$) than those we derived with the LVG analysis. Additionally, we see that the lines in these sources are optically thick. In general, the optical depth and the source size can be

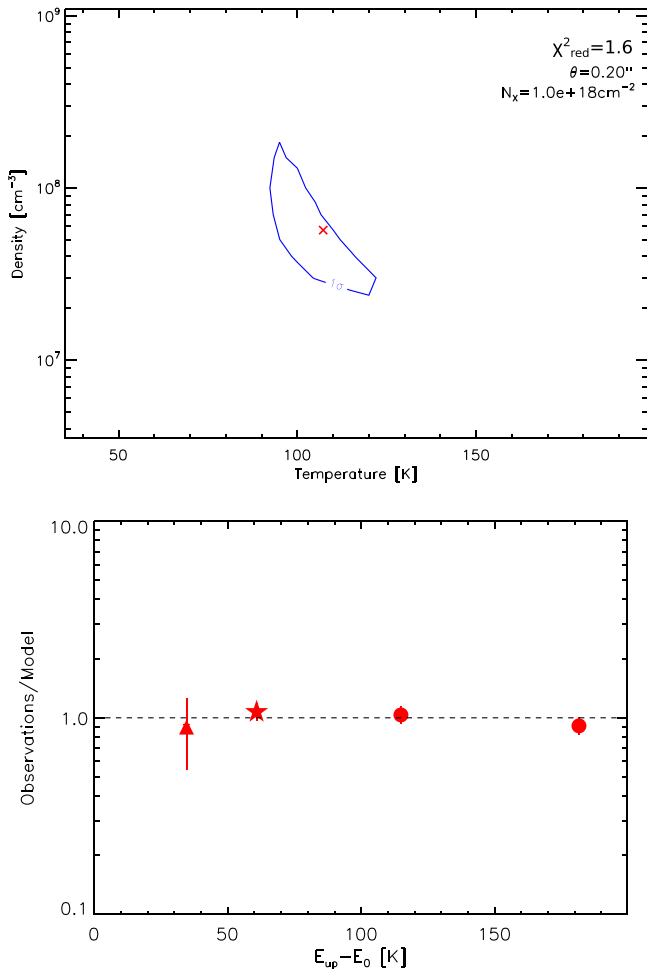


Figure 4. Result of the LVG for MMS5. Top: density–temperature χ^2 contour plot. The best-fit solution is marked by a red star and the blue contours represent the 1σ confidence level, assuming the best-fit values for $N_{\text{CH}_3\text{OH-E}}$ and θ (Table 1). Bottom: ratio between the observed line intensities with those predicted by the best-fit model as a function of the line upper-level energy E_u . Circles and stars refer to $\text{CH}_3\text{OH-E}$ and $\text{CH}_3\text{OH-A}$, respectively, while the triangle refers to the $\text{CH}_3^{18}\text{OH-A}$ detected line. E_0 is the ground rotational level energy, which is 0 K for $\text{CH}_3\text{OH-A}$ and 7.7 K for $\text{CH}_3\text{OH-E}$ (Flower et al. 2010).

corrected using the population diagram method (Goldsmith & Langer 1999). However, a population diagram cannot correct for non-LTE effects if they are present.

For each transition line, the excitation temperature corresponding to the best fit of the LVG analysis is indicated in Table B1. Comparing with the kinetic temperatures derived in the LVG analysis, we can see that some lines are subthermally populated and that there are maser lines at 218440 and 261805 MHz. We note that for CSO33-a, where the lines are optically thin and under LTE conditions, we find consistent results between the LTE and LVG analyses. For the source FIR6c-a, for which the excitation temperatures are very different from the derived kinetic temperature, we checked that non-LTE effects remain present even after correcting the rotational diagram for size and optical depth (there is still a scatter of points). In other words and as expected, the population diagram method can give a good approximation of the results if the lines are close to being thermally populated, which is only known when a non-LTE analysis is carried out.

3.4. Derivation of Methanol Abundances.

In the previous ORANGES study, we focused on the continuum analysis of the sources (Bouvier et al. 2021). We used the spectral energy distribution method to constrain several dust parameters such as the optical depth, the temperature, the H_2 column density, and the (envelope+disk) mass. These parameters were estimated for a source size derived from a fit in the visibility plane and are reported in Table 1 with the associated source size.

We therefore used these H_2 column densities to derive the methanol abundance with respect to H_2 , $X(\text{CH}_3\text{OH})$, toward each of the five sources. The results are reported in Table 1. However, because the source size derived from Bouvier et al. (2021) can be larger (up to $\sim 40\%$) than the size of the methanol emission derived from the LVG analysis, the H_2 column densities can be thus underestimated in some cases, and the derived abundances would then need to be taken as upper limits. The abundances range between 3×10^{-11} and 2×10^{-6} . For CSO33-b-a, only a lower limit could be derived for the H_2 column density, so the methanol abundance derived here is an upper limit. SIMBA-a seems to have a lower methanol abundance than the other sources but because the LVG analysis was performed with only a few data points for most of the sources, the accuracy of the fit is not very elevated.

4. Discussion

4.1. New Hot Corinos Discovered in the OMC-2/3 Filament

So far, only three hot corinos have been identified in the OMC-2/3 filament, the intermediate-mass protostars HOPS-87 and HOPS-370 (Tobin et al. 2019; Hsu et al. 2020), and HOPS-108 (Tobin & Megeath 2019; Chahine et al. 2022). One of the questions we aim to answer is: How many hot corinos are present in the OMC-2/3 filament?

Our results show that methanol is detected toward five protostars from our source sample and that the emission comes from a hot (≥ 85 K), dense ($\geq 3 \times 10^6 \text{ cm}^{-3}$), and compact ($0''.1-0''.6$ or $\sim 39-236$ au) region. According to the hot corino definition, i.e., a compact (≤ 100 au), hot (≥ 100 K), and dense ($\geq 10^7 \text{ cm}^{-3}$) region enriched in iCOMs (Ceccarelli 2004; Ceccarelli et al. 2007), CSO33-b-a, FIR6c-a, MMS9-a, MMS5, and SIMBA-a are, therefore, bona fide hot corinos.⁹ The methanol abundances derived toward the OMC-2/3 hot corinos are comparable to what is derived in other hot corinos in Orion (HOPS-87, HOPS-168, HOPS-288, G192.12-11.10, and HH 212; Lee et al. 2019; Hsu et al. 2020) and in other SFRs (e.g., B335, IRAS 16293–2422; Imai et al. 2016; Jørgensen et al. 2016, 2018), except for SIMBA-a, for which the methanol abundance is about two orders of magnitude lower. However, for FIR6c-a and MMS9-a, the abundances could be overestimated (see Section 3.4), and most of the LVG analyses were performed with only three lines. Our results should thus be taken with caution.

The five hot corinos show very different spectra as shown in Figure 5. MMS5 and MMS9-a present line-rich spectra with strong iCOM emission while CSO33-b-a, FIR6c-a, and SIMBA-a present line-poor spectra, likely because the iCOM

⁹ In this work, we targeted only CH_3OH , which is the most abundant iCOMs found in hot corinos. Other iCOMs could be also present but their identification will be the subject of a future work.

Table 1
Source Properties, LTE Results, Best-fit Results and 1σ Confidence Level (Range) from the Non-LTE LVG Analysis, and Derived Methanol Abundances with Respect to H_2

	CSO33-b-a	FIR6c-a	MMS9-a	MMS5	SIMBA-a
Source Properties ^a					
Source size [$'' \times ''$]	0.6×0.6	0.31×0.13	0.44×0.14^b	0.15×0.13	0.13×0.11
(Envelope + disk) mass [$\times 10^{-2} M_\odot$]	≥ 0.2	1.5–4	2–7	1–2	1–3
T_d [K]	10–200	89–134	80–200	149–159	160–200
H_2 [$\times 10^{24} \text{ cm}^{-2}$]	≥ 0.08	7–15	5–19	10–15	18–36
LTE Results					
Size used [$''$] ^c	0.6	0.2	0.25	0.14	0.12
T_{rot} [K]	124 ± 262	169 ± 54	142 ± 22	117 ± 14	151 ± 598
N_{tot} [$\times 10^{15} \text{ cm}^{-2}$]	13 ± 11	21 ± 6	48 ± 7	150 ± 20	20 ± 30
LVG Results					
n_{H_2} [$\times 10^7 \text{ cm}^{-3}$] best fit	300	0.4	0.7	5	1.5
n_{H_2} [$\times 10^7 \text{ cm}^{-3}$] range	≥ 20	0.3–0.5	0.6–1	2–20	≥ 0.7
T_{kin} [K] best fit	105	180	170	105	190
T_{kin} [K] range	95–120	≥ 85	≥ 130	90–125	≥ 100
$N_{\text{CH}_3\text{OH}}$ [$\times 10^{16} \text{ cm}^{-2}$] best fit	1.4	120	400	200	0.8
$N_{\text{CH}_3\text{OH}}$ [$\times 10^{16} \text{ cm}^{-2}$] range	0.7–16	80–200	200–600	140–800	0.1–3
Size [$''$] best fit	0.39	0.1	0.12	0.2	0.17
Size [$''$] range	0.1–0.6	0.07–0.13	0.1–0.13	0.13–0.24	0.08–0.38
$X(\text{CH}_3\text{OH}) \times 10^{-8d}$	≤ 200	5.3–29 ^e	10–120 ^e	9.3–80	0.003–0.2

Notes.

^a Derived from a continuum analysis in Bouvier et al. (2021).

^b Derived from a continuum analysis in Tobin et al. (2020).

^c The size is calculated using the formula $\sqrt{a \times b}$, where a and b are the major and minor axes of the source size derived in Bouvier et al. (2021).

^d The H_2 column densities can be underestimated when the source size is larger than the region of emission of methanol. The abundances derived in this work should then be taken as upper limits in these cases.

^e The methanol abundances are likely upper limits, as the source sizes used to derive the H_2 column densities are larger than the methanol emission sizes derived in the LVG analysis.

emission is faint. We will address the analysis of the other iCOMs detected toward the sources in a forthcoming paper.

4.2. Is the Dust Hiding Other Hot Corinos?

A recent study by De Simone et al. (2020) showed that hot corinos detected at centimeter wavelengths could be obscured by optically thick dust at millimeter wavelengths. Could it be the case for some of our sources?

Figure 6 shows the line intensity of the CH_3OH transition line at 243915 MHz as a function of the dust opacity. The latter has been derived for each source of the sample in Bouvier et al. (2021). For sources where no methanol is detected, we calculated the 3σ upper limit for the line intensity. If the optical depth was a dominant factor, we would expect to see an anticorrelation between the methanol intensity and τ , with the sources presenting methanol lines having the lowest range of dust optical depths. We do not see any anticorrelations, which suggests that the dust opacity is not the main parameter affecting the detection of methanol, and hence the detection of hot corinos, in the OMC-2/3 filament. However, we note that the dust optical depth ranges derived in Bouvier et al. (2021) do not always correspond to the sizes derived from the LVG analysis performed in this work. In some cases (FIR6c-a and MMS9-a), we derived methanol emission sizes that are smaller than the size of the continuum emission. This would indicate that we are underestimating the dust optical depth at the scale probed by the methanol emission. Therefore, our conclusion needs to be taken with caution. Additionally, we can see that

for four of our sample sources (MMS2-a, MMS2-b, MMS9-b, and MMS9-d), the upper limits for the derived dust optical depths are larger than 1. In these sources, we, thus, cannot exclude the possibility that the dust absorbs methanol emission at 1.3 mm.

4.3. Are ORANGES Different From PEACHES?

Several studies targeting methanol and other iCOMs toward low-mass protostars have been conducted. Yang et al. (2021) surveyed 50 sources in the Perseus Molecular cloud in the context of PEACHES. They detected CH_3OH toward 56% of their source sample and other O-bearing iCOMs toward 32% of the source sample. Belloche et al. (2020) surveyed 16 Class 0 protostars located in various low-mass SFRs as part of the Continuum And Lines in Young ProtoStellar Objects (CALYPSO) IRAM Large Program survey, with the Plateau de Bure Interferometer (PdBI; the predecessor of the current NOEMA interferometer). They detected methanol emission toward 50% of their source sample but no more than 30% of them with at least three iCOMs detected. van Gelder et al. (2020) (ALMA) surveyed seven Class 0 sources in the Perseus and Serpens molecular clouds and detected methanol toward three of them ($\sim 43\%$). Finally, Bergner et al. (2017) IRAM-30 m targeted iCOMs toward 16 Class 0/I protostars and detected the iCOMs CH_3CHO , CH_3OCH_3 , and CH_3OCHO toward 37%, 13%, and 13% of the sources, respectively. However, contrarily to the other surveys cited above, the temperatures derived by Bergner et al. (2017) being too low

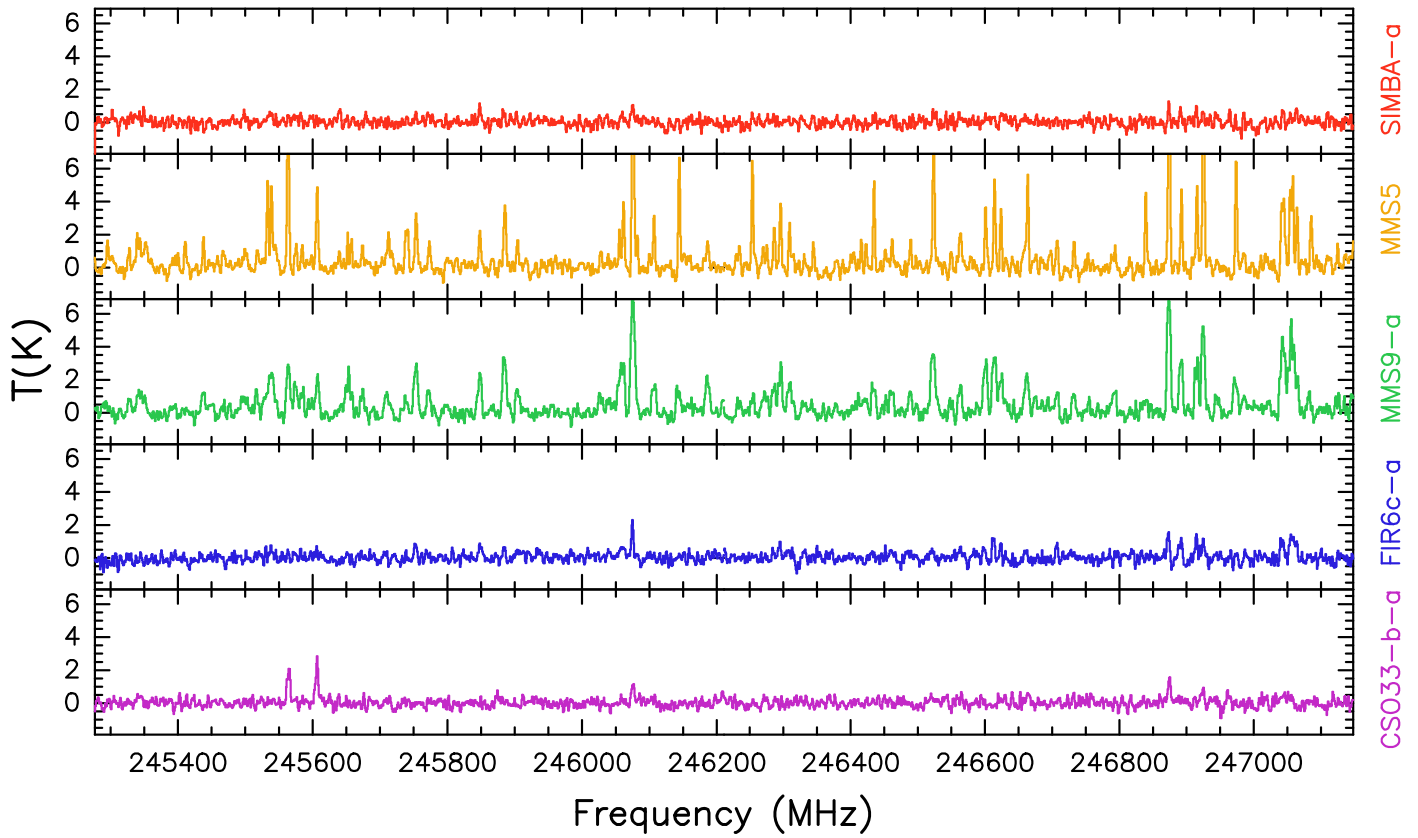


Figure 5. Spectra of each source from the large spectral window, setup 1. The spectra are extracted from a pixel at the peak of the emission.

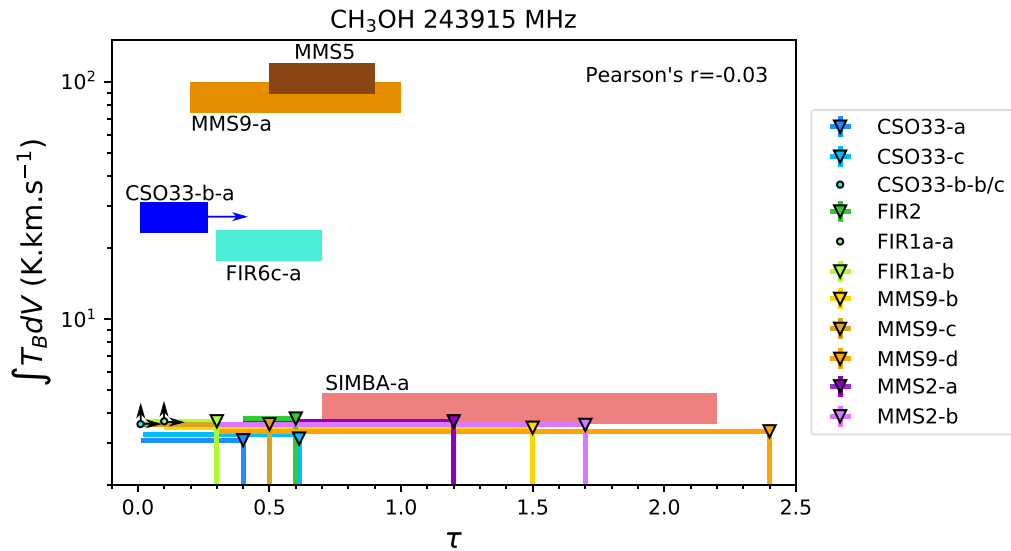


Figure 6. Line intensity of the CH_3OH line at 243915 MHz as a function of the dust optical depth, τ . For clarity, we slightly shifted vertically the upper limits for the line intensity of several sources. The initial upper limit for the CH_3OH line is 3.6 K km s^{-1} for the components of the systems CSO33 and MMS9, 3.7 K km s^{-1} for the FIR1a and MMS2 components and for CSO33-b, and 3.8 K km s^{-1} for FIR2. Upper limits are represented by colored filled triangles or arrows.

($\leq 30 \text{ K}$) for the iCOMs to originate from a hot corino region, the emission of iCOMs could trace a more external component. These surveys show that by selecting a mix of usual targets, methanol is largely detected in solar-mass protostars located in low-mass SFRs. Here, we compare our results with those of PEACHES only, as this is the only unbiased survey targeting iCOMs toward all the protostars of a single low-mass SFR. Additionally, PEACHES and ORANGES were designed to compare directly the low-mass protostellar chemical content of

two different environments, the Perseus Molecular Cloud and the OMC-2/3 filament. In both regions, the selected targets are mostly Class 0, I, or 0/I protostars with a low fraction of other (Class II or unknown) sources (7% and 11% of the sources in PEACHES and ORANGES, respectively). The relative fraction of Class 0 and I sources in each region cannot be determined accurately as the current classification of the protostars is either based on Herschel observations, for which the angular resolution is not sufficient to disentangle close multiple

systems, or not certain. However, as hot corinos are detected both toward Class 0 and I sources, this parameter is not particularly relevant when comparing the two regions. Finally, the distances of the two clouds have been taken into account to achieve the same sensitivity (~ 22 mJy beam $^{-1}$ for PEACHES and ~ 24 mJy beam $^{-1}$ for ORANGES) and spatial resolution for the two projects.

The results from PEACHES showed that $(56 \pm 14)\%$ of their source sample present warm methanol emission (Yang et al. 2021), which means that bona fide hot corinos are common in the Perseus Molecular Cloud. On the other hand, we targeted 19 solar-mass protostars located in the OMC-2/3 filament and detected only 5 bona fide hot corinos. Even though three other hot corinos are located in the OMC-2/3 filament (HOPS-87, HOPS-370, HOPS-108; Tobin & Megeath 2019; Hsu et al. 2020; Chahine et al. 2022), we do not take them into account. Indeed, unlike the above-cited studies, we performed a blind search for hot corinos using an observational setup completely analogous to that done in Perseus by Yang et al. (2021). We, thus, do not want to bias our results by adding only positive hot corino detections from other studies. Finally, using only our results, we have a hot corino detection rate of $(26 \pm 23)\%$ in the OMC-2/3 filament. Therefore, hot corinos seem to be scarcer in the OMC-2/3 filament, compared to the Perseus Molecular Cloud.

The two SFRs seem to have different chemical protostellar content but the high uncertainty for the ORANGES survey prevents us from firmly concluding. We need to increase the statistics, and to do so, a possibility would be to include the Class 0 and I populations of the OMC-4 cloud, located south of OMC-1. Additionally, as mentioned in Section 4.2, we cannot exclude that dust could hide hot corinos toward some of our source sample and, therefore, that the detection rate of 26% is underestimated. If there is truly a difference between ORANGES and PEACHES, then the environment most likely plays a role in shaping the chemical content of protostellar cores. Bounded by three H II regions, the OMC-2/3 filament is highly illuminated by ultraviolet photons, and if hot corinos are less abundant in this kind of region, it would be in line with recent modeling and observational studies (Aikawa et al. 2020; Lattanzi et al. 2020; Kalvans 2021): a cloud exposed to interstellar irradiation is very likely to be less rich in O-bearing species and in iCOMs than a more shielded one.

Although we cannot totally dismiss the possibilities that (1) some of our protostars may have small hot corino regions, preventing us from detecting iCOMs at our current resolution, and (2) high dust optical depths could still play a role in the nondetection of hot corinos in some of our sample sources, this study provides tentative evidence of differentiation of the chemical nature of solar-mass protostars that are located in two different environments or, in other words, that ORANGES may be different from PEACHES.

5. Conclusion

ORANGES aims to study the small-scale (≤ 100 au) chemical content of solar-mass protostars located in the highly illuminated OMC-2/3 filament. We detected methanol

emission centered toward five out of the 19 targeted sources. After performing a non-LTE LVG analysis, we showed that the methanol-emitting regions are hot ($T \geq 85$ K), dense ($n_{\text{H}_2} \geq 3.10^6$ cm $^{-2}$), and compact ($\sim 0''.1$ – $0''.6$ or ~ 39 – 236 au in diameter), and correspond to hot corino regions. We thus detected five new bona fide hot corinos in the OMC-2/3 filament, which corresponds to $(26 \pm 23)\%$ of the sample sources.

On the other hand, a similar study performed in the less illuminated low-mass SFR of Perseus found a high detection rate, $(56 \pm 14)\%$, of hot corinos (Yang et al. 2021). Hot corinos thus seem scarcer in a highly illuminated environment, such as the OMC-2/3 filament. This result indicates that the environment may very likely play a role in solar-mass protostars' chemical content and that ORANGES are different from PEACHES.

Are hot corinos always abundant in low-mass SFRs analog to Perseus and more scarce in analogs to the OMC-2/3 filament? We would need to perform more studies analogous to PEACHES and ORANGES in other SFRs to confirm this result. Finally, although hot corinos are present in a region similar to the one in which our Sun is born, they are not prevailing. The question of whether our Sun experienced a hot corino phase in its youth needs further investigations before being answered.

We deeply thank the anonymous referee for helpful comments that contributed to significantly improving the paper. While the paper was under review, three additional hot corinos were detected in the OMC-2/3 filament (HOPS-84-A, HOPS-84-B, and MMS1) by Hsu et al. (2022). Moreover, they targeted 56 Class 0/I protostars throughout the Orion Molecular Cloud and detected warm methanol towards $\sim 20\%$ of their sample sources, which is comparable to what we found in this work. This project has received funding from the European Research Council (ERC) under the European Union's Horizon 2020 research and innovation program, for the Project The Dawn of Organic Chemistry (DOC), grant agreement No. 741002. This paper makes use of the following ALMA data: ADS/JAO.ALMA#2016.1.00376.S. ALMA is a partnership of ESO (representing its member states), NSF (USA) and NINS (Japan), together with NRC (Canada) and NSC and ASIAA (Taiwan), in cooperation with the Republic of Chile. The Joint ALMA Observatory is operated by ESO, AUI/NRAO and NAOJ.

Appendix A Observational Details

We present here the details of the observations. Table A1 lists the targeted sources and their coordinates, and Table A2 shows the list of methanol transitions detected and used in this work and their spectral parameters. Channel spacing and primary beam size for the spectral windows containing the methanol lines are also indicated.

Table A1

Sample Sources, Coordinates of the Dust Peak Continuum (D), Coordinates of the Positions Selected to Extract the Spectra (P), Source Classification, and Associated HOPS Names

Source	R.A. (D) (J2000)	Decl. (D) (J2000)	R.A. (P) (J2000)	Decl. (P) (J2000)	HOPS name ^{a,b}	Classification ^c	Notes
CSO33-a	05:35:19.41	-05:15:38.41	HOPS-56-B	0 or I	
CSO33-b	05:35:19.48	-05:15:33.08	05:35:19.48	-05:15:33.10	HOPS-56-A-A/B/C	0	Triple system ^d
CSO33-c	05:35:19.81	-05:15:35.22	V2358 Ori	II	
FIR6c-a	05:35:21.36	-05:13:17.85	05:35:21.36	-05:13:17.85	HOPS-409	0	
FIR2	05:35:24.30	-05:08:30.74	HOPS-68	I	
FIR1a-a	05:35:24.87	-05:07:54.63	HOPS-394-B	0 or I	
FIR1a-b	05:35:24.05	-05:07:52.07	HOPS-394-A	0	
MMS9-a	05:35:25.97	-05:05:43.34	05:35:25.96	-05:05:43.39	HOPS-78-A	0	
MMS9-b	05:35:26.15	-05:05:45.80	HOPS-78-B	0 or I	
MMS9-c	05:35:26.18	-05:05:47.14	HOPS-78-C	0 or I	
MMS9-d	05:35:25.92	-05:05:47.70	HOPS-78-D	II?	
MMS5	05:35:22.47	-05:01:14.34	05:35:22.48	-05:01:14.35	HOPS-88	0	
MMS2-a	05:35:18.34	-05:00:32.96	HOPS-92-A-A/B	I	Binary ^d
MMS2-b	05:35:18.27	-05:00:33.95	HOPS-92-B	I	
CSO3-b	05:35:16.17	-05:00:02.50	HOPS-94	I	
SIMBA-a	05:35:29.72	-04:58:48.60	05:35:29.72	-04:58:48.56	HOPS-96	0	

Notes.^a Fischer et al. (2013).^b Furlan et al. (2016).^c Bouvier et al. (2021).^d Tobin et al. (2020).**Table A2**

Methanol Transition Lines Detected in this Work, Their Parameters, and Channel Spacing and Primary Beam Size of the Associated Spectral Windows

Molecule	Frequency (MHz)	Transition	E_{up} (K)	g_{up}	A_{ij} ($\times 10^{-3} \text{ s}^{-1}$)	Channel Spacing (km.s^{-1})	Primary Beam Size ($''$)
CH ₃ OH	218440	4 _{-2,3} -3 _{-1,2} E	45.5	36	4.69	0.5	28.8
	232418	10 _{2,8} -9 _{3,7} A	165.4	84	1.87	1.3	27.1
	232945	10 _{-3,7} -11 _{-2,9} E	190.4	84	2.13	1.3	27.1
	234683	4 _{2,3} -5 _{1,4} A	60.9	36	1.87	0.5	26.8
	234698	5 _{4,2} -6 _{3,3} E	122.7	44	0.63	0.5	26.8
	243915	5 _{1,4} -4 _{1,3} A	49.7	44	5.97	0.5	25.8
	261805	2 _{1,1} -1 _{0,1} E	28.0	20	5.57	0.5	24.1
	CH ₃ ¹⁸ OH	231758	5 _{0,5} -4 _{0,4} A	33.4	44	5.33	1.3

Note. Frequencies and spectroscopic parameters have been extracted from the CDMS catalog (Müller et al. 2005). For CH₃OH (TAG 032504, version 3¹) and CH₃¹⁸OH (TAG 034504, version 1¹), the available data are from Xu et al. (2008) and Fisher et al. (2007), respectively.

Appendix B**Gaussian Fit Results and CH₃¹⁸OH Spectrum**

The Gaussian fit results of the CH₃OH and CH₃¹⁸OH lines are reported in Table B1. Contaminated lines are not reported in the table as they are not included in the LVG fit. Figure B1 shows the detected transition of CH₃¹⁸OH toward MMS5.

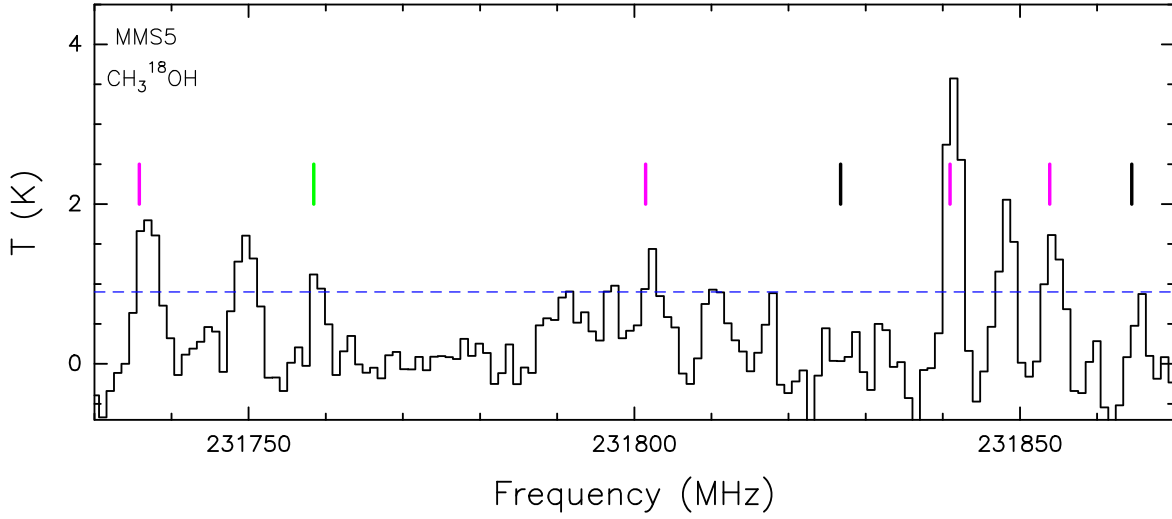


Figure B1. Spectra toward MMS5 where the frequencies of the seven $\text{CH}_3^{18}\text{OH}$ lines expected to be the most intense ($E_u < 75$ K) are indicated. Detected lines are marked in green, contaminated lines are marked in magenta, and undetected lines are marked in black. The 3σ level is indicated by the dashed blue line.

Table B1
List of Frequencies of the Detected Methanol Lines, Synthesized Beams, and Line-fitting and LVG Results

Molecule	Frequency (MHz)	Synthesized Beam MAJ($''$) \times MIN($''$) (PA{ $^\circ$ })	$\int T_B dV$ G (K km s $^{-1}$)	$\int T_B dV$ D (K km s $^{-1}$)	V_{peak} (km s $^{-1}$)	FWHM (km s $^{-1}$)	rms (K)	T_{kin} (K)	T_{ex} (K)	τ_L
CSO33-b-a										
CH_3OH	218440	0.52×0.29 (106)	18.5 ± 2.6	17.2 ± 2.2	9.4 ± 0.5	5.7 ± 0.7	0.6	105	126	6.10^{-2}
	234683	0.43×0.41 (-27)	6.0 ± 1.2	5.2 ± 1.2	8.2 ± 0.5	3.4 ± 1.0	0.4		101	$2.4 \cdot 10^{-3}$
	243915	0.32×0.28 (101)	26.8 ± 3.1	25.6 ± 2.6	9.2 ± 0.5	5.1 ± 0.5	0.4		105	9.10^{-2}
	261805	0.29×0.25 (-78)	19.4 ± 2.6	17.3 ± 2.0	9.2 ± 0.5	6.7 ± 0.7	0.5		112	4.10^{-2}
FIR6c-a										
CH_3OH	218440	0.52×0.29 (107)	10.4 ± 1.4	11.2 ± 1.3	11.2 ± 0.1	2.5 ± 0.4	0.6	180	13200	5.10^{-2}
	232945	0.48×0.27 (-71)	9.3 ± 1.4	8.9 ± 1.6	10.8 ± 0.2	4.4 ± 0.6	0.2		44.8	5.2
	234683	0.47×0.27 (109)	10.2 ± 2.2	8.6 ± 1.7	11.4 ± 0.3	3.6 ± 0.8	0.5		50.3	3.9
	234698	0.47×0.27 (109)	6.7 ± 1.5	5.2 ± 0.9	10.9 ± 0.6	3.3 ± 1.1	0.5		39.6	1.1
	243915	0.32×0.27 (-78)	22.4 ± 2.6	20.4 ± 2.2	10.7 ± 0.1	3.2 ± 0.3	0.5		169	4.8
	261805	0.30×0.25 (-77)	16.6 ± 2.6	12.1 ± 1.4	10.8 ± 0.4	4.0 ± 1.0	0.5		99.5	3.4
MMS9-a										
CH_3OH	218440	0.53×0.29 (107)	51.9 ± 5.4	51.0 ± 5.3	11.0 ± 0.5	6.7 ± 0.5	0.6	170	1130	0.9
	232945	0.49×0.27 (-71)	40.8 ± 4.4	39.2 ± 4.1	11.8 ± 1.2	7.5 ± 1.2	0.3		70.1	5.7
	234683	0.48×0.27 (109)	40.8 ± 4.6	40.0 ± 4.2	11.1 ± 0.5	6.2 ± 0.5	0.5		75	4.4
	234698	0.48×0.27 (109)	28.1 ± 3.7	27.3 ± 3.0	10.9 ± 0.5	6.1 ± 0.6	0.5		73.6	1.2
	243915	0.32×0.27 (-256)	89.6 ± 9.1	85.8 ± 8.7	11.1 ± 0.5	6.7 ± 0.5	0.5		165	7.8
	261805	0.30×0.25 (-75)	62.9 ± 6.7	60.3 ± 6.1	11.8 ± 0.5	7.0 ± 0.5	0.5		122	4.4
MMS5										
CH_3OH	218440	0.52×0.3 (107)	73.2 ± 7.4	73.9 ± 7.5	10.4 ± 0.5	3.2 ± 0.5	0.6	105	139	11.2
	232945	0.48×0.28 (-71)	52.5 ± 5.4	52.2 ± 5.2	10.3 ± 1.2	3.5 ± 1.2	0.3		93.5	4.2
	234683	0.46×0.27 (-71)	65.3 ± 6.7	65.6 ± 6.7	10.3 ± 0.5	3.2 ± 0.5	0.6		93.5	5.0
	234698	0.46×0.27 (-71)	49.2 ± 5.1	49.2 ± 5.0	10.3 ± 0.5	3.0 ± 0.5	0.6		120	0.9
	243915	0.32×0.28 (-78)	102.8 ± 10.3	103.2 ± 10.4	10.3 ± 0.5	3.4 ± 0.5	0.5		105	17.7
	261805	0.30×0.25 (-77)	96.1 ± 9.8	96.5 ± 9.9	10.3 ± 0.5	3.1 ± 0.5	1.0		110	7.6
$\text{CH}_3^{18}\text{OH}$	231758	0.48×0.28 (-71)	3.5 ± 1.3	3.3 ± 1.3	10.3 ± 1.2	2.6 ± 1.1	0.3		108	6.10^{-2}
SIMBA-a										
CH_3OH	218440	0.52×0.3 (106)	2.6 ± 0.8	3.0 ± 0.7	13.0 ± 0.3	2.0 ± 0.7	0.5	190	195	-7.10^{-2}
	243915	0.32×0.28 (-259)	4.7 ± 1.0	5.0 ± 1.0	13.2 ± 0.4	2.2 ± 0.6	0.4		172	9.10^{-2}
	261805	0.30×0.26 (-78)	1.9 ± 1.0	1.7 ± 0.6	13.1 ± 0.3	1.8 ± 0.6	0.4		3150	$-2.5.10^{-3}$

Notes. Results of the Gaussian fit (G) and of the direct integration of channel intensities (D) for the integrated intensities are reported in columns 4 and 5, respectively. The calibration uncertainty of 10% has been included in the line intensity errors. T_{kin} is the best fit for the kinetic temperature obtained from the LVG analysis, and T_{ex} and τ_L are the associated excitation temperature and line optical depth. Lines in italics are those that were not taken into account in the LTE and LVG analyses.

Appendix C

LTE Analysis: Rotational Diagrams

We show here in Figure C1, below, the rotational diagram (RD) obtained for each source. We can clearly see that the line at 45.4 K is masing and that points are scattered due to optically thick and/or non-LTE effects.

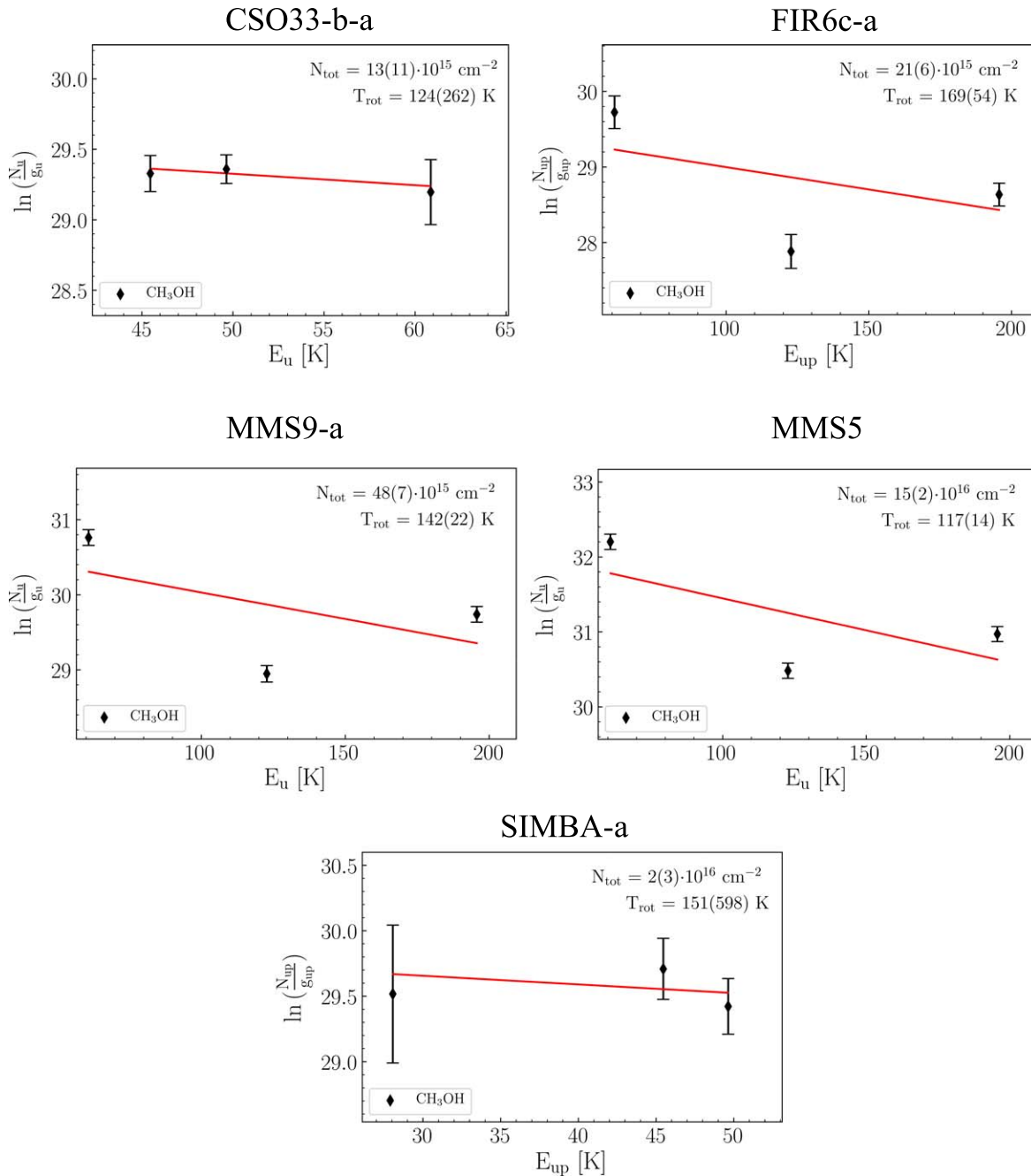


Figure C1. Rotational diagrams. Non-LTE and optically thick effects are clearly visible in FIR6c-a, MMS9-a, and MMS5, as the points are scattered throughout the plots.

ORCID iDs

Mathilde Bouvier  <https://orcid.org/0000-0003-0167-0746>
 Cecilia Ceccarelli  <https://orcid.org/0000-0001-9664-6292>
 Ana López-Sepulcre  <https://orcid.org/0000-0002-6729-3640>
 Nami Sakai  <https://orcid.org/0000-0002-3297-4497>
 Satoshi Yamamoto  <https://orcid.org/0000-0002-9865-0970>
 Yao-Lun Yang  <https://orcid.org/0000-0001-8227-2816>

References

- Adams, F. C. 2010, *ARA&A*, 48, 47
 Aikawa, Y., Furuya, K., Yamamoto, S., & Sakai, N. 2020, *ApJ*, 897, 110
 Belloche, A., Maury, A. J., Maret, S., et al. 2020, *A&A*, 635, A198
 Bergner, J. B., Öberg, K. I., Garrod, R. T., & Graninger, D. M. 2017, *ApJ*, 841, 120
 Bianchi, E., Chandler, C. J., Ceccarelli, C., et al. 2020, *MNRAS*, 498, L87
 Bianchi, E., Codella, C., Ceccarelli, C., et al. 2019, *MNRAS*, 483, 1850
 Bouvier, M., López-Sepulcre, A., Ceccarelli, C., et al. 2020, *A&A*, 636, A19
 Bouvier, M., López-Sepulcre, A., Ceccarelli, C., et al. 2021, *A&A*, 653, A117
 Ceccarelli, C. 2004, in ASP Conf. Ser. 323, Star Formation in the Interstellar Medium, ed. D. Johnstone, F. C. Adams, D. N. C. Lin et al. (San Francisco, CA: ASP), 195
 Ceccarelli, C., Caselli, P., Fontani, F., et al. 2017, *ApJ*, 850, 176
 Ceccarelli, C., Caselli, P., Herbst, E., Tielens, A. G. G. M., & Caux, E. 2007, in Protostars and Planets V, ed. V. B. Reipurth, D. Jewitt, & K. Keil (Tucson, AZ: Univ. Arizona Press), 47
 Ceccarelli, C., Maret, S., Tielens, A. G. G. M., Castets, A., & Caux, E. 2003, *A&A*, 410, 587
 Chahine, L., López-Sepulcre, A., Neri, R., et al. 2022, *A&A*, 657, A78
 Chini, R., Reipurth, B., Ward-Thompson, D., et al. 1997, *ApJL*, 474, L135
 Codella, C., Ceccarelli, C., Cabrit, S., et al. 2016, *A&A*, 586, L3
 de Jong, T., Boland, W., & Dalgarno, A. 1980, *A&A*, 91, 68
 De Simone, M., Codella, C., Ceccarelli, C., et al. 2020, *ApJL*, 896, L3
 Drozdovskaya, M. N., van Dishoeck, E. F., Rubin, M., Jørgensen, J. K., & Altwegg, K. 2019, *MNRAS*, 490, 50
 Dubernet, M.-L., Alexander, M. H., Ba, Y. A., et al. 2013, *A&A*, 553, A50
 Feddersen, J. R., Arce, H. G., Kong, S., et al. 2020, *ApJ*, 896, 11
 Fischer, W. J., Megeath, S. T., Stutz, A. M., et al. 2013, *AN*, 334, 53
 Fisher, J., Paciga, G., Xu, L.-H., et al. 2007, *JMoSp*, 245, 7
 Flower, D. R., Pineau des Forêts, G., Rabli, D., et al. 2010, *MNRAS*, 409, 29
 Furlan, E., Fischer, W. J., Ali, B., et al. 2016, *ApJS*, 224, 5
 Goldsmith, P. F., & Langer, W. D. 1999, *ApJ*, 517, 209
 Gómez-Ruiz, A. I., Gusdorf, A., Leurini, S., et al. 2019, *A&A*, 629, 77
 Großschedl, J. E., Alves, J., Meingast, S., et al. 2018, *A&A*, 619, A106
 Herbst, E., & Van Dishoeck, E. F. 2009, *ARA&A*, 47, 427
 Hsu, S.-Y., Liu, S.-Y., Liu, T., et al. 2020, *ApJ*, 898, 107
 Hsu, S.-Y., Liu, S.-Y., & Liu, T. 2022, *ApJ*, 927, 218
 Imai, M., Sakai, N., Oya, Y., et al. 2016, *ApJL*, 830, L37
 Jacobsen, S. K., Jørgensen, J. K., Di Francesco, J., et al. 2019, *A&A*, 629, A29
 Jørgensen, J. K., Müller, H. S. P., Calcutt, H., et al. 2018, *A&A*, 620, A170
 Jørgensen, J. K., van der Wiel, M. H. D., Coutens, A., et al. 2016, *A&A*, 595, A117
 Kalvans, J. 2021, *ApJ*, 910, 54
 Lattanzi, V., Bizzocchi, L., Vasyunin, A. I., et al. 2020, *A&A*, 633, A118
 Lee, C.-F., Codella, C., Li, Z.-Y., & Liu, S.-Y. 2019, *ApJ*, 876, 63
 Lis, D. C., Serabyn, E., Keene, J., et al. 1998, *ApJ*, 509, 299
 Matsushita, Y., Takahashi, S., Machida, M. N., & Tomisaka, K. 2019, *ApJ*, 871, 221
 McMullin, J. P., Waters, B., Schiebel, D., Young, W., & Golap, K. 2007, *ASPC*, 376, 127
 Müller, H. S. P., Schlöder, F., Stutzki, J., & Winnewisser, G. 2005, *JMoSt*, 742, 215
 Nielbock, M., Chini, R., & Müller, S. A. H. 2003, *A&A*, 408, 245
 Oya, Y., Sakai, N., Watanabe, Y., et al. 2017, *ApJ*, 837, 174
 Pflanzner, S., Davies, M. B., Gounelle, M., et al. 2015, *PhyS*, 90, 068001
 Rivilla, V. M., Drozdovskaya, M. N., Altwegg, K., et al. 2020, *MNRAS*, 492, 1180
 Sakai, N., Sakai, T., Hirota, T., & Yamamoto, S. 2008, *ApJ*, 672, 371
 Sakai, N., & Yamamoto, S. 2013, *ChRv*, 113, 8981
 Shimajiri, Y., Takahashi, S., Takakuwa, S., Saito, M., & Kawabe, R. 2009, *PASJ*, 61, 1055
 Takahashi, S., Saito, M., Ohashi, N., et al. 2008, *ApJ*, 688, 344
 Tanabe, Y., Nakamura, F., Tsukagoshi, T., et al. 2019, *PASJ*, 71, 8
 Tobin, J. J., Megeath, S. T., van't Hoff, M., et al. 2019, *ApJ*, 886, 6
 Tobin, J. J., Sheehan, P. D., Megeath, S. T., et al. 2020, *ApJ*, 890, 130
 van Gelder, M. L., Tabone, B., Tychoniec, L., et al. 2020, *A&A*, 639, A87
 Williams, J. P., Plambeck, R. L., & Heyer, M. H. 2003, *ApJ*, 591, 1025
 Wilson, T. L., & Rood, R. 1994, *ARA&A*, 32, 191
 Xu, L.-H., Fischer, J., Lees, R. M., et al. 2008, *JMoSp*, 251, 305
 Yang, Y.-L., Sakai, N., Zhang, Y., et al. 2021, *ApJ*, 910, 20